

The origin of pseudobulges in cosmological simulations of galaxy formation

Takashi Okamoto^{1*}

¹ *Center for Computational Sciences, University of Tsukuba, 1-1-1 Tennodai, Tsukuba 305-8577 Ibaraki, Japan*

Accepted . Received ; in original form

ABSTRACT

More than half of nearby disc galaxies have pseudobulges, instead of classical bulges that are thought to be end-products of galaxy mergers. Pseudobulges are presumed to develop over time as a result of secular evolution of galaxy discs. We report simulations of galaxy formation, in which two disc galaxies with disky pseudobulges have formed. Based on the profile decomposition, the bulge-to-total mass ratio of the simulated galaxies is 0.6 for one galaxy and 0.3 for the other. We find that the main formation mechanism of the pseudobulges in our simulations is not the secular evolution of discs but high-redshift starbursts. The progenitors of the pseudobulges form as high-redshift discs with small scale lengths by rapid supply of low angular momentum gas. The orientation of the high-redshift progenitors rapidly changes by the change of the direction of the angular momentum of newly-accreted gas, which blurs the disc properties of the high-redshift discs. Once the host haloes are well established, the direction of the angular momentum of newly-accreted gas is better aligned, and high angular momentum gas forms discs with large scale lengths. By redshift 2, before the main disc formation, pseudobulge formation has largely completed in terms of mass. The secular evolution such as bar instability accounts for about 30 % of the bulge mass for one galaxy and only ~ 13 % for the other but does affect the final shape and kinematic properties of the pseudobulges.

Key words: methods: numerical – galaxies: formation – galaxies: bulges.

1 INTRODUCTION

Pseudobulges are characterised by distinctive features from classical bulges that are thought to be merger remnants (Kormendy & Kennicutt 2004; Naab & Trujillo 2006; Hopkins et al. 2010). Pseudobulges often show substantial rotational support and disky or boxy/peanut edge-on shapes. These features support the idea that pseudobulges have formed via secular evolution of discs (Kormendy & Kennicutt 2004) caused by non-asymmetric structure in a galaxy disc such as spiral arms and a bar (e.g. Combes & Sanders 1981; Pfenniger & Norman 1990; Combes & Elmegreen 1993; Debattista et al. 2004; Athanassoula 2005) or by accretion of clumps formed in a gas rich unstable disc (Noguchi 1999; Inoue & Saitoh 2012). We call evolution that is originated by internal processes ‘secular evolution’ in this paper regardless of its timescale in order to distinguish evolution driven by external processes

such as mergers¹.

In the standard picture of galaxy formation, galaxies form via hierarchical clustering that naturally produces classical bulges. Observationally however more than half of bulges of nearby large disc galaxies are pseudobulges (Graham & Worley 2008; Weinzirl et al. 2009; Kormendy et al. 2010). This observational fact could be a challenge to the standard cosmology (Kormendy et al. 2010; Peebles & Nusser 2010). Contrarily to the intuition, cosmological simulations of Milky Way-sized galaxy formation often find that bulges show surface brightness profiles with the Sérsic indices smaller than 2 (Okamoto et al. 2005; Governato et al. 2007; Scannapieco et al. 2011; Guedes et al. 2011); such bulges are usually classified as pseudobulges (Fisher & Drory 2008, 2010; Weinzirl et al. 2009). How these bulges form over the cosmic time is

¹ Indeed, secular evolution can have timescales much shorter than a Hubble time (see Kormendy & Kennicutt 2004, for a review). Inoue & Saitoh (2012) showed that the formation timescale of a clump origin pseudobulge is rather short and they distinguished it from secular evolution.

* E-mail: tokamoto@ccs.tsukuba.ac.jp

however remain unclear.

Investigating formation processes of the simulated bulges of disc galaxies should provide important clues to understand why pseudobulges are so common both in the local Universe and simulated universes. Simulations for this purpose must resolve detailed structure of galaxies, such as shape of bulges. Only recently cosmological simulations with sufficient resolution have become possible (Okamoto & Frenk 2009; Okamoto et al. 2010; Guedes et al. 2011).

The simulations presented in this paper include a number of baryonic processes known to be relevant to galaxy formation, such as radiative gas cooling, star formation, supernova feedback, and chemical evolution. As described in Okamoto et al. (2005) and Scannapieco et al. (2011), there are many uncertainties in modelling of these ‘sub-grid’ physics. In particular, feedback is one of the most poorly understood processes, while it most strongly affects the properties of simulated galaxies (Okamoto et al. 2005, 2010; Schaye et al. 2010). We make use of a model that has already had success in reproducing some properties of the Local Group satellite galaxies, including the luminosity function and luminosity-metallicity relation (Okamoto et al. 2010) and observed properties of high-redshift Lyman- α emitters (Shimizu et al. 2011) and sub-mm galaxies (Shimizu et al. 2012).

The paper is organised as follows. In Section 2, we describe our simulations, providing brief descriptions of our modelling of baryonic processes. In Section 3, we first present properties of simulated bulges at redshift 0 to show that they have the characteristics of pseudobulges. We then show redshift evolution of the simulated galaxies and their bulges in order to address formation process of the pseudobulges. We compare our results with observations in Section 4. Finally, in Section 5, we discuss the results and summarise our main conclusions.

2 THE SIMULATIONS

To investigate the properties of Milky Way-sized galaxies, we select two of the six haloes from the Aquarius project (Springel et al. 2008): ‘Aq-C’ and ‘Aq-D’ in their labelling system. We hence assume a Λ CDM cosmology with the following parameters: $\Omega_0 = 0.25$, $\Omega_\Lambda = 0.75$, $\Omega_b = 0.045$, $\sigma_8 = 0.9$, $n_s = 0.9$, and a Hubble constant of $H_0 = 100 h \text{ km s}^{-1} \text{ Mpc}^{-1}$, where $h = 0.73$. These parameters are consistent with the WMAP 1- and 5-year results at the 3σ level (Spergel et al. 2003; Komatsu et al. 2009). These haloes are extracted from a cosmological periodic box of the side length of $100 h^{-1} \text{ Mpc}$, and were chosen to have masses close to that of the Milky Way’s dark matter halo ($\sim 10^{12} M_\odot$). These haloes are relatively isolated and do not have neighbours exceeding half its mass within $1 h^{-1} \text{ Mpc}$ (Navarro et al. 2010).

As in Aquarius, we use the resimulation technique; the initial density field of the parent simulation is recreated

by adding appropriate additional short wavelength perturbations in the region out of which the halo of interest forms. In this region, we also place gas particles which are used to perform Smoothed Particle Hydrodynamic (SPH) calculation. The region external to this is populated with high-mass dark matter particles, the function of which is to reproduce the appropriate tidal fields.

The high-resolution dark matter particle mass is $2.6 \times 10^5 M_\odot$ and $2.2 \times 10^5 M_\odot$, respectively for Aq-C and Aq-D, and the original SPH particle mass is thus $5.8 \times 10^4 M_\odot$ and $4.8 \times 10^4 M_\odot$. Note that the SPH particle mass can change owing to star formation and feedback. Gravitational softening length is kept constant in comoving coordinates as $\epsilon = 1.03 \text{ kpc}$ until redshift 3, and then fixed in physical coordinates as $\epsilon = 0.257 \text{ kpc}$ in both simulations. We adopt the same softening length for the high-resolution dark matter, gas, and star particles.

2.1 The simulation code

The simulation code is based on an early version of a Tree-PM SPH code, GADGET-3 and it is exactly the same as the one used in (Parry et al. 2012). The baryonic processes are modelled so as to reproduce the properties of the Local Group satellite galaxies (Okamoto & Frenk 2009; Okamoto et al. 2010). The simulations include metallicity dependent radiative cooling and photoheating (Wiersma et al. 2009) in the presence of a time-evolving, spatially uniform ultraviolet background (Haardt & Madau 2001). The star formation occurs in dense gas with $n_H > n_{\text{th}}$, where n_{th} is the threshold gas density above which the star formation is enabled. The star formation efficiency is set to reproduce the Kennicutt relation (Kennicutt 1998) as described in Okamoto et al. (2008) (see also G3-TO model in Scannapieco et al. 2012). The simulations include both Type II and Ia supernovae and follow the evolution of the chemical elements produced by these two types of supernovae and by AGB stars.

Energetic feedback from supernovae explosion is modelled as winds (Springel & Hernquist 2003; Oppenheimer & Davé 2006; Okamoto et al. 2008; Dalla Vecchia & Schaye 2008). When a gas particle receives an amount of energy ΔE from Type II supernovae during a timestep, Δt , this particle is added to winds with a probability, $p_w = \Delta E / (\frac{1}{2} m_{\text{gas}} v_w^2)$, where m_{gas} is the mass of the SPH particle and v_w is the initial wind speed. This is given as $v_w = 5\sigma$, where σ is the one-dimensional velocity dispersion of the dark matter particles around the gas particle (vw5 σ model in Okamoto et al. 2010). The wind particles are decoupled from the hydrodynamic calculation for a short time in order to allow them to escape the high-density star-forming regions. When the density has fallen to $n_H = 0.01 \text{ cm}^{-3}$, the particles feel the usual hydrodynamic force again. If they do not reach sufficiently low densities after a time $10 \text{ kpc}/v_w$, they are recoupled to the hydrodynamic interactions anyway.

This expression of the wind mass-loading implies that the wind mass generated by a Type II supernova is proportional to σ^{-2} , i.e. per unit of star formation, less

massive galaxies blow more winds than their more massive counterparts. This is a key feature to reproduce properties of the Local Group satellites, including the shape and approximate normalisation of their luminosity function and the luminosity-metallicity relation (Okamoto et al. 2010).

The model for supernovae driven winds used here differs from the original one by Okamoto et al. (2010) in two ways. Firstly, we allow all gas particles, not just those above the star formation threshold density, to be added to the wind if they receive feedback energy. The original prescription can result in a variable wind mass-loading depending on how well the star-forming region is resolved. Secondly, only type II supernovae contribute to the winds. Type Ia supernova energy is added to the gas as thermal energy.

There are several more changes to the code from the one used in the previous studies. Firstly, the star formation threshold density is now a function of the numerical resolution while it was fixed to $n_H = 0.1 \text{ cc}^{-1}$ in the previous studies. For the resolution of the simulations presented in this paper, we employ $n_H = 1.6 \text{ cc}^{-1}$ as the star formation threshold density (see Appendix. B for more details). Secondly, we have implemented a timestep limiter (Saitoh & Makino 2009) that reduces the timestep of a gas particle if it is too long compared to the neighbouring gas particles. Without this limiter, halo gas particles which have much longer timesteps than high-speed wind particles often do not feel the force from the wind particles (i.e. do not notice the wind particles), while the wind particles feel the drag from the surrounding halo gas particles. Lastly, we have added artificial conductivity in order to capture the instabilities at contact surfaces (Price 2008) together with the time dependent artificial viscosity (Morris & Monaghan 1997); otherwise SPH cannot deal with such instabilities (Okamoto et al. 2003; Agertz et al. 2007). All these changes have significantly improved the numerical convergence as we show in Appendix B (see also Parry et al. 2012).

3 RESULTS

In this section, we first analyse the properties of the simulated galaxy bulges in order to show that the simulated disc galaxies have pseudobulges. We then show the evolution of the galaxies and their bulges to understand pseudobulge formation. The global properties of the simulated galaxies at redshift 0 are summarised in Appendix A. In the following analyses, the z -direction is chosen to be parallel to the angular momentum vector of stars within 5 % of the virial radius² at given redshift. Note that the direction of the angular momentum vector significantly changes with redshift (Okamoto et al. 2005; Scannapieco et al. 2009; Sales et al. 2012) as we will show later. The x -direction is to be parallel to the major axis of the surface stellar density distribution in face-on. We also define galaxy radius as 10 % of the virial radius.

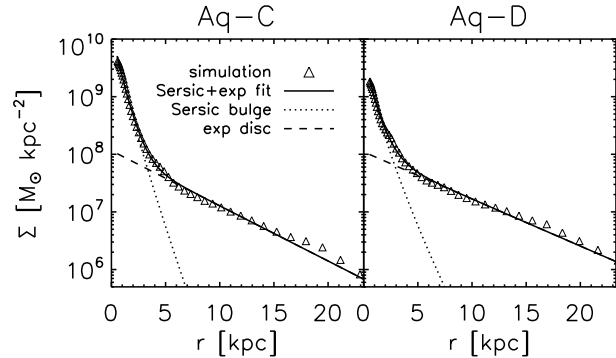


Figure 1. Azimuthally averaged surface stellar density profiles. The left and right panels show profiles of Aq-C and Aq-D galaxies, respectively. The profiles of each galaxy is fitted by a combination of the Sérsic and exponential profiles. The surface density profiles are indicated by the triangles and the best fit profiles are shown by the solid lines. The contribution from Sérsic bulges (dotted lines) and the exponential discs (dashed lines) are also plotted. The bulges are well fitted by the Sérsic indices, $n \simeq 1.2$ and 1.4 , for Aq-C and Aq-D, respectively.

3.1 Shapes and kinematic properties of the bulges

For classifying bulges, the Sérsic profile fitting for a surface stellar density profile is frequently used:

$$\Sigma(r) = \Sigma_e \exp \left[-b_n \left\{ \left(\frac{r}{R_e} \right)^{\frac{1}{n}} - 1.0 \right\} \right], \quad (1)$$

where R_e is the effective radius and Σ_e is the surface density at R_e , respectively, and n is the Sérsic index. The parameter b_n is related to n by $b_n \simeq 2n - 0.324$. Bulges with $n < 2$ are usually classified as pseudobulges (Kormendy & Kennicutt 2004; Fisher & Drory 2008, 2010; Weinzierl et al. 2009)³. In Fig. 1, we show the surface density profiles from face-on (x - y projection) of the simulated galaxies at redshift 0. We fit each profile by a combination of the Sérsic bulge and exponential disc profiles. We obtain $n \simeq 1.2$ and 1.4 for the bulges of Aq-C and Aq-D, respectively. These bulges hence have pseudobulge-like profiles. According to the profile fitting, the bulge-to-total mass ratios, B/T , are 0.6 for Aq-C and 0.3 for Aq-D. These values suggest that Aq-C is an early-type disc galaxy and Aq-D is presumably classified as an Sb galaxy. The bulge stars dominate mass within 3 kpc from the galaxy centres; more than 92 % and 86 % for Aq-C and Aq-D, respectively. We thus regard this region as a bulge.

In Fig.2, we show the face-on (upper panels) and edge-on (lower panels) surface stellar density maps. From the face-on density maps, it is evident that Aq-C has a bar, while Aq-D shows almost axisymmetric surface stellar density distribution except in the central region ($r < 2$ kpc) where we see weak non-axisymmetry. In the edge-on density maps, both bulges appear to be quite ‘flat’. This is not what one would expect for a classical bulges; both

² The virial radius is calculated based on the spherical collapse model (Eke et al. 1996)

³ Note that this classification at $n = 2$ was questioned by Graham (2011) because bulges ranging from $n = 0.5$ to 10 obey a single curved relation in the $R_e - n$ plane.

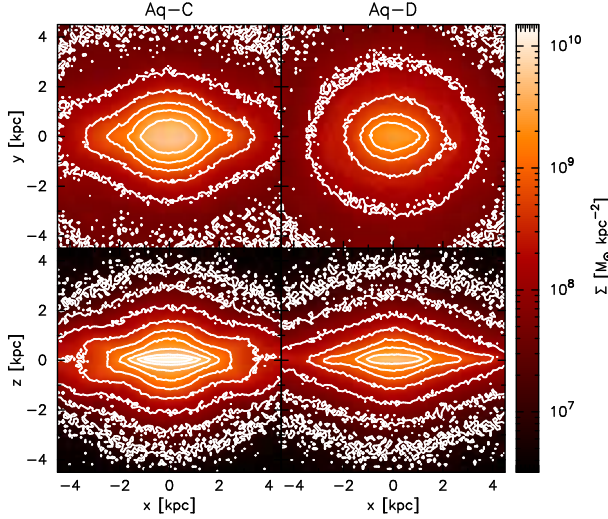


Figure 2. Surface stellar density maps of the bulges. The upper panels show the face-on views (x - y projection) and the lower panels show the edge-on views (x - z projection). The contour levels are chosen to highlight the bulge shapes, which are clearly ‘disky’ in the edge-on views.

galaxies seem to possess ‘disc-like’ bulges (Athanasoula 2005, or ‘disky pseudobulges’ in Erwin 2008’s terminology). A further evidence for a dominant central disk-like structure is the diamond shaped isodensity contours in Aq-D’s bulge (Pohlen et al. 2000). The inner part of Aq-C’s bulge also shows disk-like, diamond isodensity contours, while the outer part has ‘boxy’ features ($2 \lesssim |x| \lesssim 4.5$ kpc and $1 \lesssim |z| \lesssim 2$ kpc). The boxy/peanut shape is related to bar structure (Athanasoula 2005) and therefore the boxy isodensity contours are consistent with the fact that Aq-C has a bar.

Next we investigate the kinematic properties of the simulated bulges. In the top panels of Fig. 3, we show the mean line-of-sight velocity maps from edge-on view. Both bulges have significant rotation but the shapes of the isovelocity contours are rather different between them; Aq-C’s contours are more vertical than Aq-D’s, implying the rotation properties of Aq-C’s bulge is more cylindrical. This is presumably due to the presence of the bar.

We plot the line-of-sight velocity profiles (rotation curves) at the disc plane ($|z| < 0.1$ kpc) in the middle panels and the line-of-sight velocity dispersion profiles in the bottom panels. We find that the inner part of Aq-C’s bulge is rather kinematically hot; the velocity dispersion profiles are sharply peaked at $x = 0$. The region is supported by the velocity dispersion of the stars rather than the rotation. We also plot the vertical (z -direction) velocity dispersion of the stars in the disc plane. The vertical velocity dispersion is only half the line-of-sight one. Therefore the orbits of stars in the inner part of the bulge are largely non-circular but confined in a thin oblate. On the other hand, Aq-D’s bulge is kinematically cold. The line-of-sight velocity dispersion profile is very flat and it seems typical of the disk-like pseudobulges (Erwin 2008). The cold, highly rotationally supported fea-

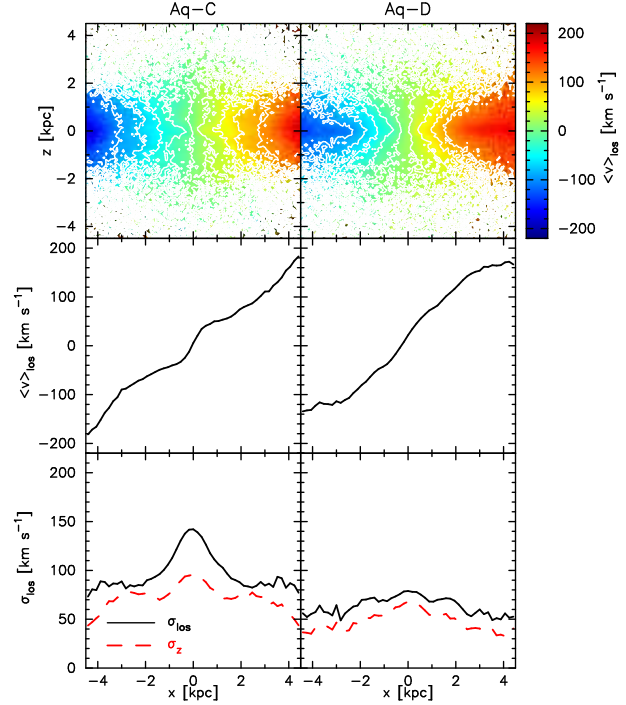


Figure 3. Kinematic properties of the bulges from edge-on view (x - z projection). *Top panels:* The mean line-of-sight velocity maps. The contour levels correspond to $|\langle v_{\text{los}} \rangle| = 0, 25, 50, 75, 100, 150$ km s $^{-1}$. *Middle panels:* The line-of-sight velocity profiles at the disc plane ($|z| < 0.1$ kpc). *Bottom panels:* The line-of-sight velocity dispersion profiles at the disc plane. We also show the vertical (z -direction) velocity dispersion profiles at the disc plane by the red dashed lines.

ture of the bulge implies that the pseudobulge is a disc-like bulge.

3.2 Evolution of the galaxies and their bulges

In this subsection we investigate how the galaxies and their bulges form and evolve in the simulations. Fig. 4 shows stellar and gas distribution in the main progenitors of Aq-C and Aq-D galaxies around redshift 3, 2, 1, 0.5, and 0. Again we chose the z -direction to be parallel to the angular momentum vector and x -direction to the major axis. At redshift 3, both galaxies show irregular morphology, characterised by an inner disc and misaligned outer disc or ring. The misalignment is caused by the change of the direction of angular momentum vector of newly accreted gas as we will show later. The components that eventually evolve into the discs at redshift 0 start forming around redshift 2. Aq-C forms a bar around redshift 1 and the bar survives until redshift 0. In Aq-D, a weak (and short) bar-like feature can be seen at redshift 2, which disappears by redshift 1. Aq-D’s late-time evolution below redshift 1 is characterised by clumpy star formation.

Our main result is depicted in Fig. 5 where we show the surface stellar density profiles of the main progenitor galaxies from face-on view at several redshifts. Redshift evolution of the surface density profiles indicates that a high-redshift disc with a small scale length forms first,

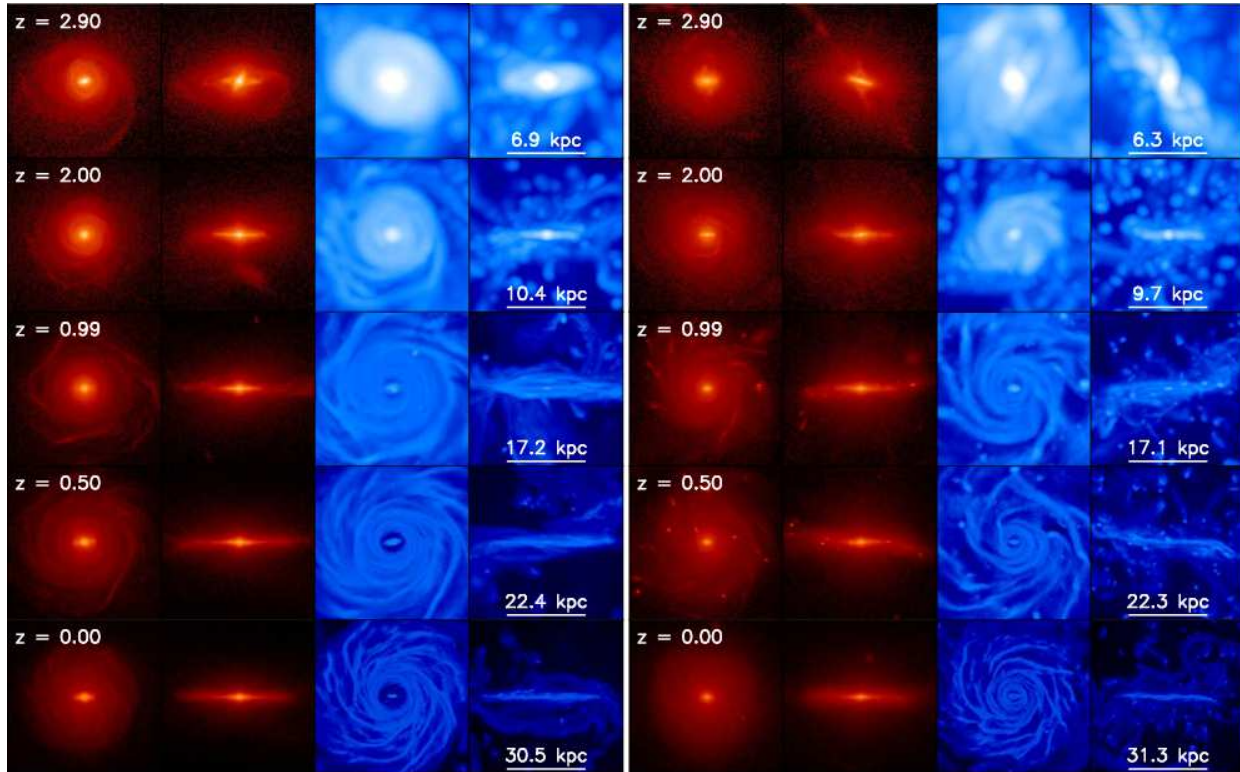


Figure 4. Evolution of the galaxies. The side length of each panel is set to 20 % of the virial radius of the host dark matter halo at a given redshift. The galaxy radius which is defined as 10 % of the virial radius is indicated by a horizontal line in each panel. The left and right concatenated panels, respectively, show Aq-C and Aq-D galaxies. From left to right, the surface stellar density in face-on (x - y projection) and in edge-on (x - z), and surface gas density in face-on and in edge-on are presented. Brighter colour is used for higher density. From top to bottom, we show the main progenitor at redshift 2.9, 2.0, 0.99, 0.5, and 0. The z -direction is chosen to be parallel to the angular momentum of stars within 5 % of the virial radius at each redshift. The x -direction is to be parallel to the major axis as in Fig. 2 and 3.

then a component that eventually evolves into the disc at redshift 0 develops around it. In fact, the Sérsic bulges are always disc-like ($n < 2$). It is evident that there has been only a little evolution in the bulge mass since redshift 2; the bulge mass at redshift 2 already accounts for ~ 70 % of that at redshift 0 for Aq-C and ~ 87 % for Aq-D. Because the discs seen at redshift 0 start forming around redshift 2, we conclude that the main channel of the pseudobulge formation in our simulations is not secular evolution of the main (or outer) discs, although secular evolution seems to have non-negligible contribution (~ 30 %) to the mass of Aq-C's bulge, which is the one that has the bar at low redshift.

In Fig. 6, we present the formation histories of bulge stars: the stars lie within 3 kpc from the galaxy centres at redshift 0. In order to distinguish the stars that born in the main progenitor (*in situ*) from that brought by accreted satellites (*accreted*), we identify subhaloes by using SUBFIND (Springel et al. 2001) and construct merger trees. We define subhaloes as systems that consists of at least 32 self-bound particles. To identify clumps formed by the self-gravitational instability of gas (see Aq-D in Fig. 4), we also utilise SUBFIND; a group of self-bound particles that contains more than 32 particles found within the galaxy radius, $0.1r_{\text{vir}}$, whose baryon fraction is more than 90 % is

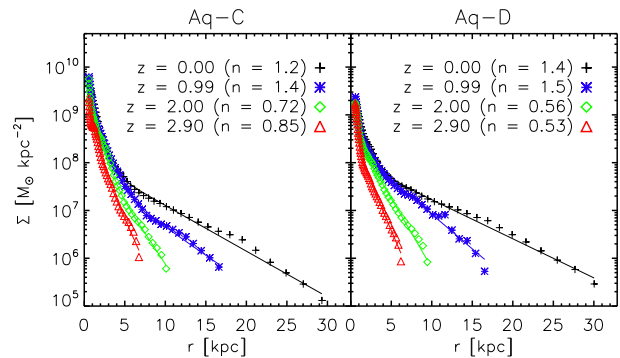


Figure 5. Evolution of the surface stellar density profiles. The surface stellar density profiles of Aq-C (left) and Aq-D (right) galaxies and their main progenitors obtained from face-on views are presented. The profiles around redshift 0, 1, 2, and 3 are indicated by the black plus signs, blue asterisks, green diamonds, and red triangles, respectively. Each profile is fitted by a combination of a Sérsic bulge and an exponential disk, which is shown by the line. The Sérsic indices are shown in each panel.

regarded as a clump.

As shown in the top panels of Fig. 6, most of the bulge stars are born in starbursts between redshifts 2 and 6 in

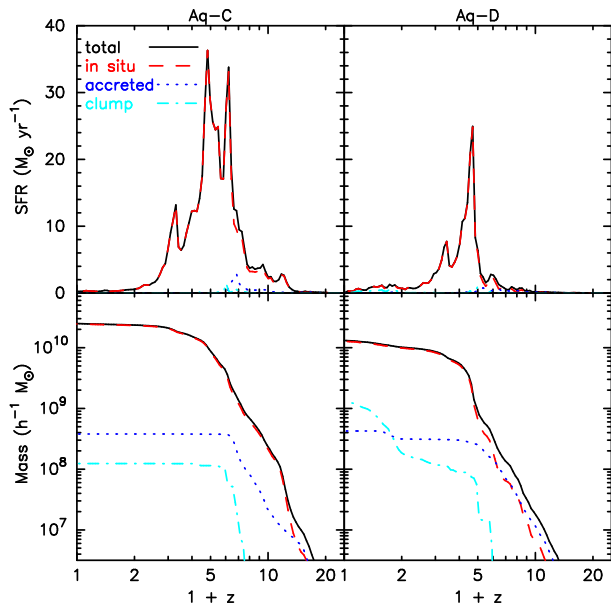


Figure 6. Distribution of formation times of bulge stars expressed in terms of redshift. Stars lie within 3 kpc from the galaxy centre at redshift 0 are identified as the bulge stars here. The left and right panels show Aq-C and Aq-D galaxies, respectively. The upper and lower panels show the same data in differential and cumulative form, respectively. The black solid lines indicate all the bulge stars, while the red dashed and blue dotted lines respectively indicate those born in the main progenitors (*in situ*) and those born in the satellites (*accreted*). The cyan dot-dashed lines show *in situ* stars which have formed in gas clumps.

Aq-C and between 2 and 4 in Aq-D. Moreover, most of the bulge stars are *in situ*. This fact implies at least ‘dry mergers’ do not contribute to the formation of the bulges. There is little star formation activity below redshift 1 in Aq-C’s bulge, while Aq-D’s bulge show slight activity at low redshift. We find that about half the star formation in Aq-D’s bulge below redshift 1 occurs in the gas clumps. The clumps sink to the galaxy centre by dynamical friction and add mass to the bulge (Inoue & Saitoh 2012). However, the contribution from the clumps is only about 10 % and not as large as in the ‘clump origin pseudobulge’ reported by Inoue & Saitoh (2012).

In order to investigate what triggers the starbursts, we first analyse the star formation and merging histories of the galaxies. We define galaxy mass, M_{gal} , as the sum of the stellar mass, M_* , and the interstellar medium (ISM) mass, M_{ISM} , in a subhalo, where we regard the gas with high density ($n_{\text{H}} > 0.1 \text{ cc}^{-1}$) and low temperature ($T < 3 \times 10^4 \text{ K}$) as the ISM. The star-forming gas ($n_{\text{H}} > 1.6 \text{ cc}^{-1}$) is also counted as the ISM. The merging mass ratio is defined by the second massive progenitor to the main progenitor mass in a merger.

In the upper panel of Fig. 7, we show the star formation histories of stars within the galaxy radius at redshift 0 and the merging mass ratios. We find that the star formation activity is not strongly correlated with mergers with some exceptions in Aq-C: the starbursts at redshifts ~ 5.5 and 2 might be triggered by the mergers. We also find that

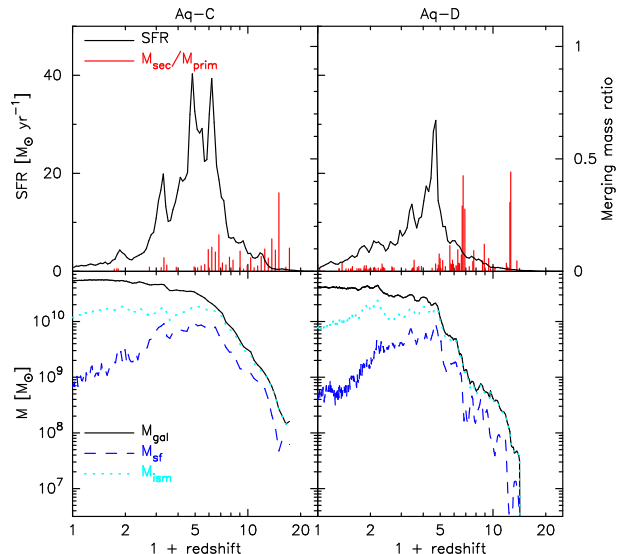


Figure 7. Star formation and merging histories of the simulated galaxies. The left and right panels show evolution of Aq-C and Aq-D, respectively. *Upper panels:* Star formation histories of the stars within the galaxy radius ($0.1r_{\text{vir}}$) at redshift 0 are shown by the black lines. The red vertical lines indicate merging mass ratios. All the mergers whose mass ratios are greater than 0.01 are presented. Note that the number of outputs of Aq-D simulation is as four times larger as that of Aq-C simulation; hence the number of the vertical lines is larger for Aq-D. *Lower panels:* Mass evolution of the main progenitor galaxies. The total (stellar + ISM), star-forming gas, and ISM masses in the main progenitor of each galaxy are shown by the black solid, blue dashed, and cyan dotted lines, respectively.

both galaxies have not undergone mergers with mass ratio greater than 0.1 since redshift 4.

We present the mass evolution of the galaxies and the mass in the ISM and star-forming gas as functions of redshift in Fig. 7. The mass evolution indicates that the galaxies are quite gas rich until the first starbursts at redshift ~ 5 for Aq-C and at redshift ~ 3.5 for Aq-D since our feedback effectively suppresses star formation in small galaxies. The major mergers at high redshift are thus *wet*; wet mergers are not as destructive as dry ones (Hopkins et al. 2010) and sometimes form discs by depositing orbital angular momentum (Springel & Hernquist 2005; Robertson et al. 2006; Governato et al. 2009). The gas richness at high redshift seems to prevent the galaxies from forming classical bulges.

Roughly speaking, the starbursts above redshift 2 establish the pseudobulges (see Fig. 6) and therefore the quiescent star formation below redshift 2 seen in the star formation histories of the galaxies as a whole (Fig. 7) builds up the discs, although there are some star formation activities at low redshift in Aq-D’s bulge. Since mergers are not correlated with the star formation activity, starbursts seem to be triggered by the rapid supply of low angular momentum gas. Indeed, the galaxy masses are dominated by the ISM when they grow rapidly as shown in the lower panels of Fig. 7. This suggests that gas accretion

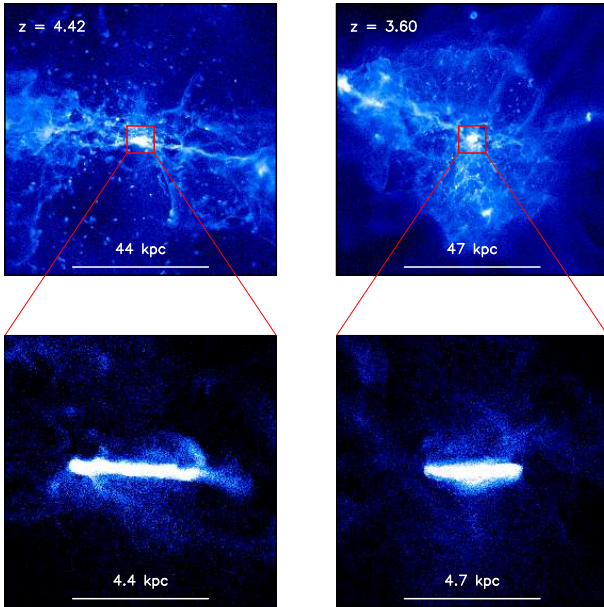


Figure 8. Gas distribution during starbursts from edge-on views. The left and right panels respectively show gas distribution in and around Aq-C at redshift 4.42 and Aq-D at redshift 3.65 at which the galaxies have the highest star formation rates. *Upper panels:* Projected gas density in a cube of side length $2r_{\text{vir}}$ is shown. The brightness scales with the projected gas density. The virial radii, r_{vir} , are indicated by the horizontal lines. *Lower panels:* Same as in the upper panels but the side length of the cube is $0.2r_{\text{vir}}$. The galaxy radii, $0.1r_{\text{vir}}$, are also indicated by the horizontal lines.

is much faster than star formation. We also show the gas distribution in and around the main progenitors when the galaxies have the highest star formation rate, redshift 4.42 for Aq-C and 3.60 for Aq-D in Fig. 8. It reveals that gas is supplied along the dense filaments that penetrate the host haloes⁴ and the starbursts occur in the unperturbed gas discs.

The formation of the pseudobulges ends by gas consumption due to the starbursts and supernova feedback modelled as winds that remove the star-forming gas from the central region; subsequently, high angular momentum gas gets accreted and forms discs with large scale length. At this epoch, the haloes are well established and the angular momentum of the accreting gas is better aligned. This is how two distinctive disk components, namely the pseudobulges and the discs, form in our simulations. The evolution of the baryonic mass in the host haloes provides further support to this scenario, which we present in the next subsection.

3.3 Evolution of the host haloes

Here we investigate the evolution of the main progenitor haloes and their mass content. We illustrate the mass evolution of the main progenitor haloes of Aq-C and Aq-D in Fig. 9. In the upper panels, we show the mass in dark matter, stars, star-forming gas, warm gas, and hot gas as

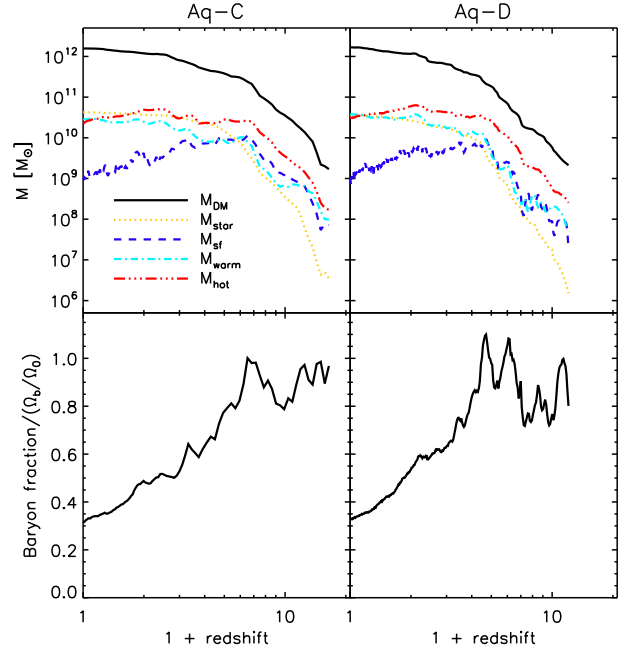


Figure 9. Mass evolution of the main progenitor haloes. *Upper panels:* The mass content in the main progenitor haloes as a function of redshift. The black solid, yellow dotted, blue dashed, cyan dot-dashed, and red dot-dot-dot-dashed lines indicate mass in dark matter, stars, star-forming gas, warm gas, and hot gas, respectively. *Lower panels:* Evolution of the baryon fractions in the main progenitor haloes. The baryon fractions are normalised by the cosmic mean baryon fraction, Ω_b/Ω_0 .

functions of redshift, where the star-forming gas is high density gas ($n_{\text{H}} > n_{\text{th}} = 1.6 \text{ cc}^{-1}$), hot gas is that with $T > 10^5 \text{ K}$ or that in the winds, and we define the rest as warm gas.

Both haloes have virial mass of $\sim 10^{12} M_{\odot}$ at redshift 0 as we chose the haloes of the Milky Way’s halo mass. The fractions of baryons locked into stars, i.e. $M_{\text{star}}/[M_{\text{vir}}(\Omega_b/\Omega_0)]$, are 0.15 and 0.11, respectively for Aq-C and Aq-D and are in reasonable agreement with the observation (Guo et al. 2010; Behroozi et al. 2010; Moster et al. 2010) as shown in Appendix A. The amount of the star-forming gas becomes largest at redshift ~ 5 in Aq-C and at redshift ~ 3.5 in Aq-D. Below these redshifts the mass of the star-forming gas monotonically decreases with decreasing redshift owing to the star formation and feedback.

The effect of winds is depicted in the lower panels of Fig. 9 in which we plot the baryon fraction in the main progenitor haloes. The baryon fraction is normalised by the cosmic mean value Ω_b/Ω_0 , that is, if a halo has not lost any baryons, the value becomes unity. The baryon fraction is high at high redshift and decreases towards lower redshift owing to the winds. There is an interesting feature between redshift 5–9 in Aq-C and 3.5–7 in Aq-D, where the baryon fractions increase towards lower redshift. At these redshifts, the haloes glow rapidly and the gas inflow competes the outflow. Consequently, the baryon fractions are peaked at redshift ~ 5 in Aq-C and at redshifts ~ 3.5

⁴ This is what called ‘cold mode’ accretion by Kereš et al. (2009).

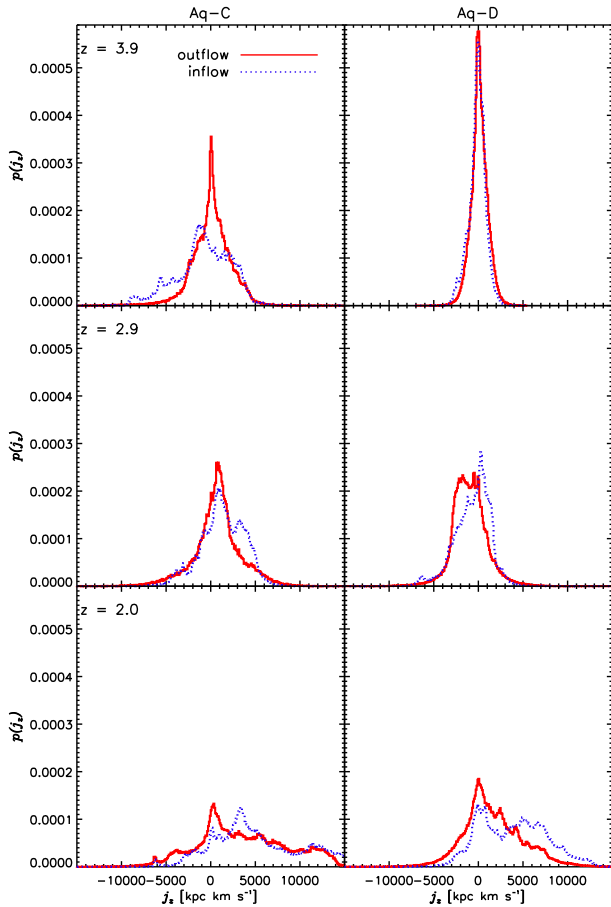


Figure 10. Distribution of angular momentum of outflows and inflows. Outflows (inflows) are defined as gas moving radially outward (inward) between $0.3r_{\text{vir}}$ and $0.7r_{\text{vir}}$. The red solid and blue dotted lines indicate outflows and inflows, respectively. From top to bottom, the distributions at redshift $\simeq 4$, 3, and 2 are shown.

in Aq-D. These redshifts coincide with the redshifts at which the mass of the star-forming gas becomes largest; the starbursts occur at these epochs. The baryon fractions then sharply drop because strong supernova feedback following the starbursts blow out the gas from the haloes. During the quiescent star formation (redshift < 2), the baryon fractions keep decreasing and they are only one third of the cosmic mean at redshift 0. After the first starbursts, the total baryon mass in the haloes are almost constant, while the baryon fractions decreases. This means that the mass flux in outflows balances that in the inflows. The outflows preferentially remove low angular momentum gas (Governato et al. 2010; Brook et al. 2011); on the other hand, low-redshift inflows in general bring in high angular momentum gas. The complicated interplay between inflows and outflows forms two disk components with different scale length.

Fig. 10 shows the distribution of angular momentum of inflows and outflows during the starbursts. Outflows (inflows) are defined as gas moving radially outward (inward) between $0.3r_{\text{vir}}$ and $0.7r_{\text{vir}}$ where wind particles have already been recoupled to the hydrodynamic interactions. The z -direction is chosen as the direction of the spin of the galaxy

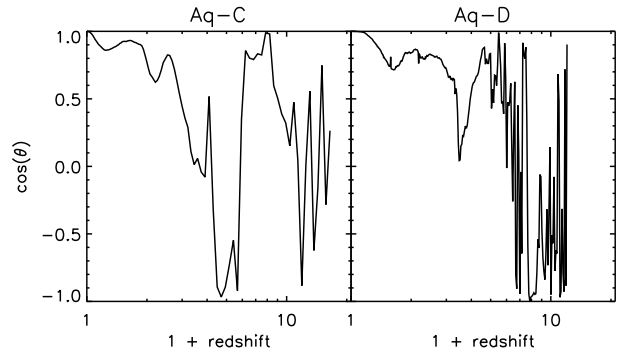


Figure 11. Spin flips: Evolution of the orientation of the galaxies. The cosine of the angle between the direction of the spin of the galaxy at redshift 0 and that of the main progenitor at each redshift is plotted in each panel. The direction is computed using the stellar component within $0.5r_{\text{vir}}$, where stars in the satellites are removed from the analysis.

at a given redshift. We find that the angular momentum distributions of the outflows are always peaked at $j_z = 0$ showing that the outflows consist of low angular momentum gas. The inflows at redshift 4 show strange behaviour; the net rotation of the inflows in Aq-C is retrograde and is almost zero in Aq-D. We will show the reason for this in Section 3.4. At redshift < 3 , the distribution of the angular momentum of the inflows show peaks at $j_z > 0$. The outflows however remove a large amount of high angular momentum gas too. Feedback and star formation prescriptions that remove low angular momentum gas more efficiently would yield smaller bulges (see Guedes et al. 2011; Macciò et al. 2012).

3.4 Orientation and rotation of the galaxies and their bulges

During the growth of a dark halo, the direction of its spin undergoes rapid changes (Bett & Frenk 2012). The direction of the angular momentum vector of newly accreting gas also changes dramatically. This induces the ‘flip’ of a disc (Okamoto et al. 2005) and sometimes destroyed a preexisting disc (Scannapieco et al. 2011). Sales et al. (2012) pointed out, by using GIMIC simulations (Crain et al. 2009), that many bulges in Milky Way-sized haloes form owing to this misalignment of newly-accreted gas.

In Fig.11, we show the evolution of the galaxy orientation. We define the spin of a disc by using the direction of the angular momentum vector of the stellar component within $0.5r_{\text{vir}}$, where we ignore the stars in satellites to avoid misdefining the galaxy orientation due to the orbital angular momentum of the satellites. The orientation of the galaxies rapidly changes at high redshift by the change of the direction of the angular momentum vector of newly-accreted materials.

The flips displayed in Fig. 11 cause to form the misaligned discs for example seen at redshift 3 in Fig. 4. However, the pseudobulges are perfectly aligned to the discs at redshift 0 in spite of the fact that most of the bulge stars have formed before redshift 2. How such misalignments are dissolved is displayed in Fig. 12, where we plot the

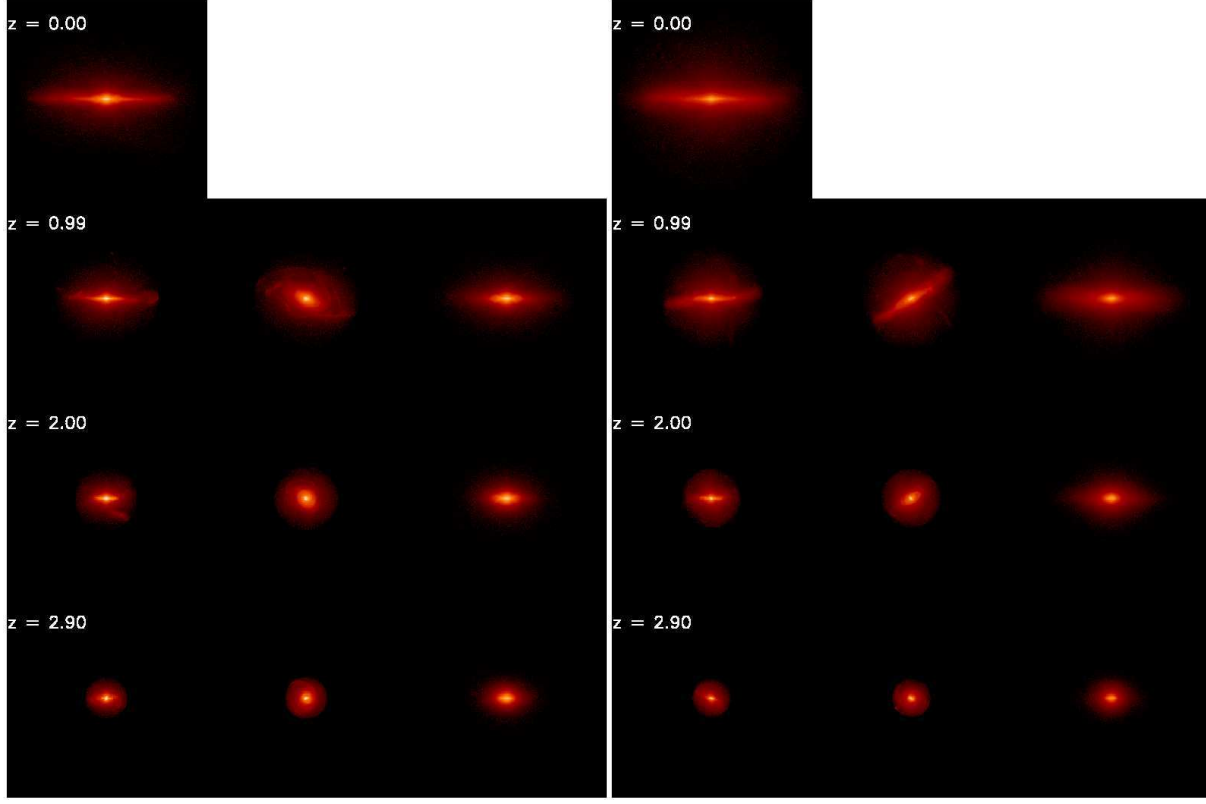


Figure 12. Distribution of the stars in the main progenitors at several redshifts and their distribution at redshift 0. The left concatenated panels are for Aq-C and the right for Aq-D. From top to bottom, we show the surface stellar density in the galaxies at redshift 0, 0.99, 2.0, and 2.9. *Left panels:* The surface stellar density of the main progenitors, the viewing angles are chosen to be edge-on at given redshifts. *Middle panels:* Same as the left panels but the viewing angles are chosen to be edge-on for the galaxies at redshift 0 (The same viewing angle as in the top-left panel). *Right panels:* The surface density of the stars in the galaxies at redshift 0 which consist the high-redshift progenitors in the same row. The viewing angles are chosen to be edge-on at redshift 0, i.e. the same viewing angles as in the middle panels. The side length of the each panel is 65 kpc.

distribution of the stars in the main progenitors at several redshifts. The left panels show the edge-on views of the main progenitors, while in the middle panels the viewing angles are chosen to be edge-on for the galaxies at redshift 0, that is, the viewing angles are the same as in the top-left panels. These panels indicate that the high-redshift discs are indeed significantly misaligned with their descendants at redshift 0. However if we look at how the stars in the high-redshift progenitors distribute at redshift 0, they are well aligned to the discs at redshift 0 as shown in the right panels, where we plot the stars at redshift 0 that consist the high-redshift progenitors and the viewing angles are chosen to be edge-on for the galaxies at redshift 0 (the same viewing angles as in the middle panels). This suggests that a preexisting disc exchanges its angular momentum with newly-accreted misaligned materials that have higher angular momentum and then align with a new disc. During the course of the rearrangement, the stars in a preexisting disc are strongly disturbed and settle into a hotter disc. As a result, the discs shown in the right panels in Fig. 12 is much thicker than those in the corresponding left panels.

The same information is shown in Fig. 13 more quantitatively, where we plot the component of the specific angular momentum of the stars in the main progenitors

at redshift $\simeq 1, 2$, and 3 that is parallel to the angular momentum vector of the galaxies at redshift 0, and that of the same set of the stars at redshift 0 (j_{\parallel} at given redshifts and redshift 0). We also show the magnitude of the specific angular momentum of the stars in the main progenitors and that of the same set of the stars at redshift 0 ($|j|$ at given redshifts and redshift 0). The offset of j_{\parallel} from $|j|$ seen for the high-redshift progenitors indicates that they are misaligned with the galaxies at redshift 0. At redshift 0, the stars in these progenitors get perfectly aligned with the galaxies at redshift 0 because j_{\parallel} is equal to $|j|$ at redshift 0 for all the high-redshift progenitors. Since newly-accreted materials torque the stars in the progenitors, j_{\parallel} increases towards redshift 0. This is not always the case for $|j|$. In Aq-C, the magnitude of the specific angular momentum of the stars that consist the high-redshift progenitors decreases towards redshift 0. On the other hand it increases in Aq-D. This difference might be originated by the different late-time evolution of their bulges, which is driven by a bar in Aq-C and by sinking clumps in Aq-D.

To highlight the difference in the late-time evolution, we show the ratios of the mean rotation speed to the velocity dispersion of the stars v_{rot}/σ within 0.1 kpc from the disc plane at several redshifts in Fig. 14. Note that the definitions

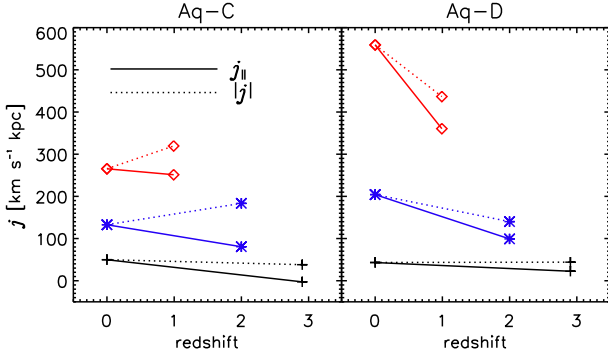


Figure 13. Evolution of the specific angular momentum of the stars that consist the high-redshift main progenitors. The main progenitors at redshift 0.99, 2.0, 2.9 are represented by the red diamonds, blue asterisks, and black plus signs, respectively. The component of the specific angular momentum parallel to the angular momentum of the galaxies at redshift 0 is connected by the solid line and the magnitude of the specific angular momentum is connected by the dotted line.

of the rotation speed and that of the velocity dispersion are different from those in Fig. 3. Here the rotation speed is the azimuthally averaged tangential velocity and the velocity dispersion is the rms average between the tangential and radial velocity dispersions. The $v_{\text{rot-to-}\sigma}$ ratio of Aq-C within the bulge ($r \lesssim 3$ kpc) has significantly decreased since redshift 1. We have inspected the rotation speed and velocity dispersion profiles separately and have confirmed that the decrease is caused by the decrease of the rotation speed, not by the increase of the velocity dispersion. The loss of the rotation support is probably driven by the bar, that is, the angular momentum of the stars in the bar is transferred mainly to the dark matter. In fact, the pattern speed of the bar at redshift 0 is only one third of that at redshift 1. Investigating the evolution of the bar and its influence to the galaxy is beyond the scope of this paper and we defer it to a forthcoming paper. In contrast, v_{rot}/σ of Aq-D does not change significantly below redshift 1. We have confirmed that both the rotation speed and velocity dispersion profiles have not changed much in the bulge region since redshift 1. This fact provides further support to the speculation that Aq-C's bulge has lost the rotation support owing to the bar.

4 COMPARISON WITH OBSERVATIONS

In this section, we compare the simulated galaxies and bulges with observations. We firstly investigate whether the simulated galaxies are too bulge-dominated to host pseudobulges or not. Galaxies with pseudobulges are in general have smaller B/T than those with classical bulges (e.g. Graham & Worley 2008; Fisher & Drory 2008; Fisher et al. 2009; Weinzirl et al. 2009). For example Fisher & Drory (2008) showed that most of the galaxies with pseudobulges have $B/T < 0.4$ in V-band and $\simeq 0.5$ at a maximum; Fisher et al. (2009) reported that such galaxies have $B/T < 0.6$ in near-IR; All high-mass ($M_* \geq 10^{10} M_\odot$) spirals whose bulge indices are smaller than 2 have H-band $B/T \lesssim 0.4$ (Weinzirl et al. 2009). In our simulations, the values of H-band B/T are 4.6

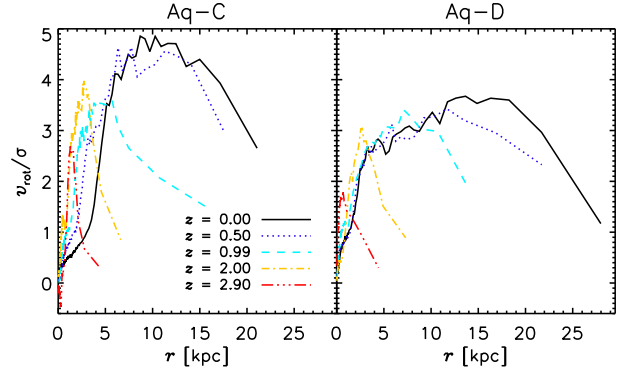


Figure 14. Ratio of rotation speed to velocity dispersion of stars as a function of radius. The left and right panel show Aq-C and Aq-D, respectively. We measure the ratio of the mean rotation speed to velocity dispersion of stars within 0.1 kpc from the disk plane ($|z| < 0.1$ kpc). The black solid, blue dotted, cyan dashed, yellow dot-dashed, and red dot-dot-dot-dashed lines respectively represent the main progenitors at redshift around 0, 0.5, 1, 2.0, and 3. Here the definition of the rotation speed and that of the velocity dispersion are different from those in Fig. 3. The rotation speed is azimuthally averaged tangential velocity and the velocity dispersion is the rms average between the tangential and radial velocity dispersions.

and 2.1 for Aq-C and Aq-D, respectively⁵. Therefore Aq-C's B/T value is on the very high end of what has been observed and it might be out of range because we ignore the dust extinction which reduces the disc luminosity.

Next, we compare the specific star formation rate in the bulges with observed values. Following Fisher et al. (2009), the bulge radius, R_{XS} , is defined as the radius at which the surface stellar density profile of a bulge is 25 % higher than that of a disc. The bulge mass, M_{XS} , is then given as:

$$M_{\text{XS}} = M_{\text{star}}(< R_{\text{XS}}) - 2\pi\Sigma_0 \int_0^{R_{\text{XS}}} r e^{-r/R_d} dr. \quad (2)$$

We list the bulge mass, the bulge radius, the star formation rate internal to the bulge, \dot{M}_{XS} , and the specific star formation rate of the bulge, $\dot{M}_{\text{XS}}/M_{\text{XS}}$, in Table 1. The specific star formation rates, $1.1 \times 10^{-11} \text{ yr}^{-1}$ (Aq-C) and $1.4 \times 10^{-11} \text{ yr}^{-1}$ (Aq-D), are in good agreement with those for the *inactive* pseudobulges (Fisher et al. 2009). Pseudobulge formation via high-redshift starbursts provides a good explanation for the formation of such inactive pseudobulges.

Bulges of nearby galaxies are however less massive than $10^{10} M_\odot$ (Fisher et al. 2009). Aq-C's bulge ($M_{\text{XS}} = 2.2 \times 10^{10}$) seems to be too massive. This is because that the simulated galaxies have too much star formation at high redshift. Aq-C has formed half of the final stellar mass by redshift 3.3 and Aq-D by redshift 1.8. Leitner (2012) argued that current star-forming galaxies formed most of their stellar mass at redshift lower than 2. Results from abundance matching also show that Aq-C forms too many stars at redshift higher than 2 (Moster et al. 2012, their Fig. 12) for its

⁵ B/T becomes smaller in bluer bands (see also Table. A1)

Table 1. Size, mass and star formation rate of the simulated bulges at redshift 0.

Galaxy	R_{XS} (kpc)	M_{XS} (M_{\odot})	\dot{M}_{XS} ($M_{\odot} \text{ yr}^{-1}$)	$\dot{M}_{\text{XS}}/M_{\text{XS}}$ (yr^{-1})
Aq-C	3.2	2.2×10^{10}	2.4×10^{-1}	1.1×10^{-11}
Aq-D	2.7	7.6×10^9	1.1×10^{-1}	1.4×10^{-11}

halo mass. The disagreement at high redshift indicates possible failure of our galaxy formation model. We will discuss effects of this early star formation in Section 5.

5 SUMMARY AND DISCUSSION

We have performed N -body/hydrodynamic simulations of galaxy formation in two Milky Way-sized haloes in a Λ CDM universe. The haloes are taken from the Aquarius project (Springel et al. 2008): Aq-C and Aq-D. Both galaxies form well defined discs; one has the bulge-to-total mass ratio, $B/T \simeq 0.6$, and the other, $B/T \simeq 0.3$, based on the surface stellar density profiles. The Sérsic index of Aq-C’s bulge is 1.2 and that of Aq-D’s bulge is 1.4. These values suggest that both bulges are ‘pseudobulges’. The edge-on surface stellar density maps confirm that these bulges indeed show the characteristics of pseudobulges, they particularly resemble ‘disky pseudobulges’, while Aq-C also has features of a ‘boxy bulge’. The boxiness is consistent with the existence of a bar in Aq-C (Athanasoula 2005).

The formation histories of these pseudobulges are rather different from the standard picture, in which pseudobulges are believed to form through secular evolution of galaxy discs. In our simulations, the pseudobulges mainly form by high-redshift starbursts before redshift 2. The evolution of the surface stellar density profiles reveals that the pseudobulge components are already in place at redshift 2–3 as disk-like components with small scale length. The mass of these central disk components at redshift 2 accounts for $\sim 70\%$ and $\sim 87\%$ of the final pseudobulge mass of Aq-C and Aq-D, respectively. These progenitors of the pseudobulges would be observed as high-redshift discs (Stark et al. 2008). In fact, when the galaxies have peak star formation rates, the star formation occurs in unperturbed gas discs. The high-redshift discs continuously change the orientation by exchanging the angular momentum with newly-accreted materials whose angular momentum is misaligned with the preexisting discs. In the course of the frequent flips, the discs are heated and turn into pseudobulge-like objects.

The main stage of the formation of the pseudobulges ends soon after the starbursts by gas consumption due to the starbursts and the energetic winds that removes star-forming gas. When the host haloes are well established, the gas cooled in the haloes has larger angular momentum and gradually develops the discs with larger scale length than the pseudobulges. The secular evolution of the main discs that is mainly driven by bar instability in Aq-C and clumpy star formation in Aq-D further increases the mass of the pseudobulges. The secular evolution however accounts for only $\sim 30\%$ and $\sim 13\%$ of the mass of the pseudobulges

of Aq-C and Aq-D, respectively. We therefore conclude that the main channel of the pseudobulge formation in our simulations is *not* the secular evolution of the discs.

The specific star formation rates of the simulated bulges are consistent with those of the observed inactive pseudobulge (Fisher et al. 2009), implying that such pseudobulges have formed via high-redshift starbursts. The bulge mass, Aq-C’s bulge in particular, is however too large to compare with the observed counterparts. Aq-C indeed shows too much early star formation before redshift 2 (Moster et al. 2012). We are thus likely to overestimate the importance of the high-redshift starbursts for pseudobulge formation especially for Aq-C.

There seems to be two reasons why the simulated galaxies do not form classical bulges. One is that the host haloes have relatively quiet merger histories as described in Wang et al. (2011). Consequently, the galaxies have not undergone mergers with mass ratios greater than 0.1 since redshift 4. The merging mass ratios of the galaxies becomes smaller than those of their host haloes owing to the feedback which is more effective in smaller galaxies. The other reason is that when the galaxies are quite gas rich when they undergo major mergers at high redshift. This is again due to our feedback that suppresses star formation very efficiently when the main progenitors are small. Wet (gas rich) mergers are not as destructive as dry (collisionless) mergers (Hopkins et al. 2010) and often form discs as merger remnants (Springel & Hernquist 2005; Robertson et al. 2006; Governato et al. 2009). Any successful simulations of disc galaxy formation must suppress early star formation (Brook et al. 2004; Okamoto et al. 2005; Guedes et al. 2011; Scannapieco et al. 2012); we thus speculate that gas richness in high-redshift progenitors is the key to explain the high fraction of pseudobulges in nearby large disc galaxies.

The formation scenario of pseudobulges by high-redshift starbursts presented in this paper provides a good explanation for the existence of pseudobulges in early-type disc galaxies such as S0 and Sa galaxies. Pseudobulges do exist in early-type disc galaxies (Kormendy & Kennicutt 2004) and secular evolution may take too long to form such large pseudobulges. In our simulations, large pseudobulges with the bulge-to-total mass ratios, $B/T \sim 0.6$ and ~ 0.3 ; $\sim 70\%$ and $\sim 87\%$ of them have formed through high-redshift starbursts, respectively, and secular evolution adds the rest. A simulation of a smaller galaxies $M_{\text{gal}} \sim 10^{10} M_{\odot}$, for which feedback is more efficient than in Milky Way-sized galaxies, showed that its pseudobulge has formed by the secular evolution Brook et al. (2012). We hence expect that different formation processes of pseudobulge operate depending on galaxy mass.

ACKNOWLEDGEMENTS

I would like to thank Shigeki Inoue, Junich Baba, and Daisuke Kawata for stimulating discussion. The simulations were performed with T2K Tsukuba at Centre for Computational Sciences in University of Tsukuba. This work was

supported in part by Grant-in-Aid for Scientific Research (S) by JSPS (20224002), by Grant-in-Aid for Young Scientists (B: 24740112), and by MEXT HPCI STRATEGIC PROGRAM.

REFERENCES

- Abadi M. G., Navarro J. F., Steinmetz M., Eke V. R., 2003, *ApJ*, 597, 21
- Agertz O., et al., 2007, *MNRAS*, 380, 963
- Athanassoula E., 2005, *MNRAS*, 358, 1477
- Behroozi P. S., Conroy C., Wechsler R. H., 2010, *ApJ*, 717, 379
- Bett P. E., Frenk C. S., 2012, *MNRAS*, 420, 3324
- Brook C. B., et al., 2011, *MNRAS*, 415, 1051
- Brook C. B., Kawata D., Gibson B. K., Flynn C., 2004, *MNRAS*, 349, 52
- Brook C. B., Stinson G., Gibson B. K., Roškar R., Wadsley J., Quinn T., 2012, *MNRAS*, 419, 771
- Combes F., Elmegreen B. G., 1993, *A&A*, 271, 391
- Combes F., Sanders R. H., 1981, *A&A*, 96, 164
- Crain R. A., et al., 2009, *MNRAS*, 399, 1773
- Dalla Vecchia C., Schaye J., 2008, *MNRAS*, 387, 1431
- Debattista V. P., Carollo C. M., Mayer L., Moore B., 2004, *ApJL*, 604, L93
- Eke V. R., Cole S., Frenk C. S., 1996, *MNRAS*, 282, 263
- Erwin P., 2008, in *IAU Symposium*, Vol. 245, *IAU Symposium*, M. Bureau, E. Athanassoula, & B. Barbuy, ed., pp. 113–116
- Fisher D. B., Drory N., 2008, *AJ*, 136, 773
- , 2010, *ApJ*, 716, 942
- Fisher D. B., Drory N., Fabricius M. H., 2009, *ApJ*, 697, 630
- Governato F., et al., 2010, *Nat*, 463, 203
- , 2009, *MNRAS*, 398, 312
- Governato F., Willman B., Mayer L., Brooks A., Stinson G., Valenzuela O., Wadsley J., Quinn T., 2007, *MNRAS*, 374, 1479
- Graham A. W., 2011, *ArXiv e-prints*, 1108.0997
- Graham A. W., Worley C. C., 2008, *MNRAS*, 388, 1708
- Guedes J., Callegari S., Madau P., Mayer L., 2011, *ApJ*, 742, 76
- Guo Q., White S., Li C., Boylan-Kolchin M., 2010, *MNRAS*, 404, 1111
- Haardt F., Madau P., 2001, in *Clusters of Galaxies and the High Redshift Universe Observed in X-rays*, Neumann D. M., Tran J. T. V., eds.
- Hopkins P. F., et al., 2010, *ApJ*, 715, 202
- Inoue S., Saitoh T. R., 2012, *MNRAS*, 422, 1902
- Kennicutt Jr. R. C., 1998, *ApJ*, 498, 541
- Kereš D., Katz N., Fardal M., Davé R., Weinberg D. H., 2009, *MNRAS*, 395, 160
- Komatsu E., et al., 2009, *ApJS*, 180, 330
- Kormendy J., Drory N., Bender R., Cornell M. E., 2010, *ApJ*, 723, 54
- Kormendy J., Kennicutt Jr. R. C., 2004, *ARA&A*, 42, 603
- Leitner S. N., 2012, *ApJ*, 745, 149
- Macciò A. V., Stinson G., Brook C. B., Wadsley J., Couchman H. M. P., Shen S., Gibson B. K., Quinn T., 2012, *ApJL*, 744, L9
- Morris J. P., Monaghan J. J., 1997, *Journal of Computational Physics*, 136, 41
- Moster B. P., Naab T., White S. D. M., 2012, *ArXiv e-prints*, 1205.5807
- Moster B. P., Somerville R. S., Maubetsch C., van den Bosch F. C., Macciò A. V., Naab T., Oser L., 2010, *ApJ*, 710, 903
- Naab T., Trujillo I., 2006, *MNRAS*, 369, 625
- Navarro J. F., et al., 2010, *MNRAS*, 402, 21
- Noguchi M., 1999, *ApJ*, 514, 77
- Okamoto T., Eke V. R., Frenk C. S., Jenkins A., 2005, *MNRAS*, 363, 1299
- Okamoto T., Frenk C. S., 2009, *MNRAS*, 399, L174
- Okamoto T., Frenk C. S., Jenkins A., Theuns T., 2010, *MNRAS*, 406, 208
- Okamoto T., Jenkins A., Eke V. R., Quilis V., Frenk C. S., 2003, *MNRAS*, 345, 429
- Okamoto T., Nemmen R. S., Bower R. G., 2008, *MNRAS*, 385, 161
- Oppenheimer B. D., Davé R., 2006, *MNRAS*, 373, 1265
- Parry O. H., Eke V. R., Frenk C. S., Okamoto T., 2012, *MNRAS*, 419, 3304
- Peebles P. J. E., Nusser A., 2010, *Nat*, 465, 565
- Pfenniger D., Norman C., 1990, *ApJ*, 363, 391
- Pohlen M., Dettmar R.-J., Lütticke R., Schwarzkopf U., 2000, *A&AS*, 144, 405
- Price D. J., 2008, *Journal of Computational Physics*, 2271, 10040
- Robertson B., Bullock J. S., Cox T. J., Di Matteo T., Hernquist L., Springel V., Yoshida N., 2006, *ApJ*, 645, 986
- Saitoh T. R., Makino J., 2009, *ApJL*, 697, L99
- Sales L. V., Navarro J. F., Theuns T., Schaye J., White S. D. M., Frenk C. S., Crain R. A., Dalla Vecchia C., 2012, *MNRAS*, 423, 1544
- Scannapieco C., et al., 2012, *MNRAS*, 423, 1726
- Scannapieco C., White S. D. M., Springel V., Tissera P. B., 2009, *MNRAS*, 396, 696
- , 2011, *MNRAS*, 417, 154
- Schaye J., et al., 2010, *MNRAS*, 402, 1536
- Shimizu I., Yoshida N., Okamoto T., 2011, *MNRAS*, 418, 2273
- , 2012, *ArXiv e-prints*, 1207.3856
- Sofue Y., Honma M., Omodaka T., 2009, *PASJ*, 61, 227
- Spergel D. N., et al., 2003, *ApJS*, 148, 175
- Springel V., Hernquist L., 2003, *MNRAS*, 339, 289
- , 2005, *ApJL*, 622, L9
- Springel V., et al., 2008, *MNRAS*, 391, 1685
- Springel V., White S. D. M., Tormen G., Kauffmann G., 2001, *MNRAS*, 328, 726
- Stark D. P., Swinbank A. M., Ellis R. S., Dye S., Smail I. R., Richard J., 2008, *Nat*, 455, 775
- Wang J., et al., 2011, *MNRAS*, 413, 1373
- Weinzirl T., Jogee S., Khochfar S., Burkert A., Kormendy J., 2009, *ApJ*, 696, 411
- Wiersma R. P. C., Schaye J., Smith B. D., 2009, *MNRAS*, 393, 99

Table A1. Mass and morphology of the simulated galaxies at redshift 0. The stellar mass, M_{star} , and the i -band luminosity, M_i , of the galaxies are computed by using the stars within the galaxy radius. We present the best fit values of the parameters for the Sérsic bulges and explanation discs: Σ_e , R_e and n in equation (1), the disc central surface stellar density, Σ_d , and the disc scale length, R_d . We also show the i -band bulge-to-total luminosity ratio, $(B/T)_i$.

Galaxy	$M_{\text{star}} (M_\odot)$	M_i (mag)	$\Sigma_e (M_\odot \text{ kpc}^{-2})$	R_e (kpc)	n	$\Sigma_0 (M_\odot \text{ kpc}^{-2})$	R_d (kpc)	$(B/T)_i$
Aq-C	4.0×10^{10}	-21.3	2.2×10^9	0.98	1.2	1.2×10^8	4.5	0.38
Aq-D	3.1×10^{10}	-21.2	7.2×10^8	1.1	1.4	1.1×10^8	5.3	0.22

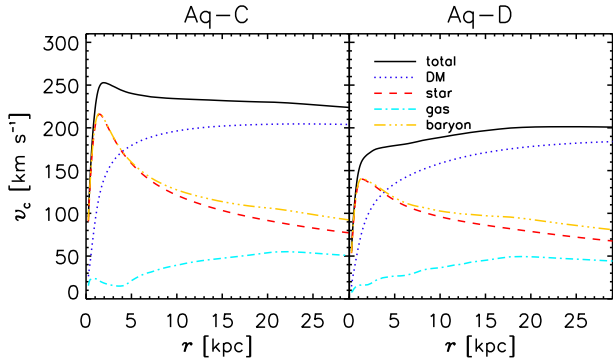


Figure A1. Circular velocity profiles at redshift 0. The circular velocity profiles, $v_c(r) = \sqrt{GM(<r)}/r$, are shown by the black solid lines. The blue dotted, red dashed, cyan dot-dashed, and yellow dot-dot-dot-dashed lines respectively indicate the contribution from the dark matter, stellar, gas, and baryonic (stellar plus gas) components.

APPENDIX A: PROPERTIES OF THE SIMULATED GALAXIES AT REDSHIFT 0

We here give some of the key properties of our simulated galaxies at redshift 0. In Table A1, we show the mass and i -band luminosity of them. We also present the best fit values of the parameters in the surface stellar density profile fitting. For reference, we also show the i -band bulge-to-total luminosity ratios, $(B/T)_i$, which take lower values than the mass ratios because the discs contains more young stars than the bulges. The disc scale lengths seem to be too large compared with a typical value with observed galaxies of similar types (a few kpc). Such morphological details are quite sensitive to the implementation of star formation and feedback and beyond the scope of this paper.

In Fig. A1, we show the circular velocity profiles. Note that the circular velocity, $v_c \equiv \sqrt{GM(<r)}/r$, is different from the rotation speed presented in Fig. 3 and 14. We find that the circular velocity profiles are very flat and the values are consistent with the Milky Way's value ($\sim 200 \text{ km s}^{-1}$; Sofue et al. 2009, see also G3-TO model in Scannapieco et al. 2012). The stellar component dominates within $\sim 4 \text{ kpc}$. Therefore within the bulges, stars dominate in mass and the outer region, where the discs exist, is dominated by dark matter.

In Fig. A2, we show how many baryons in the haloes are locked into stars. Behroozi et al. (2010), Guo et al. (2010) and Moster et al. (2010) have pointed out only 20% of baryons in a halo are locked into stars at most. Guo et al. (2010) showed the great majority of simulations lock too

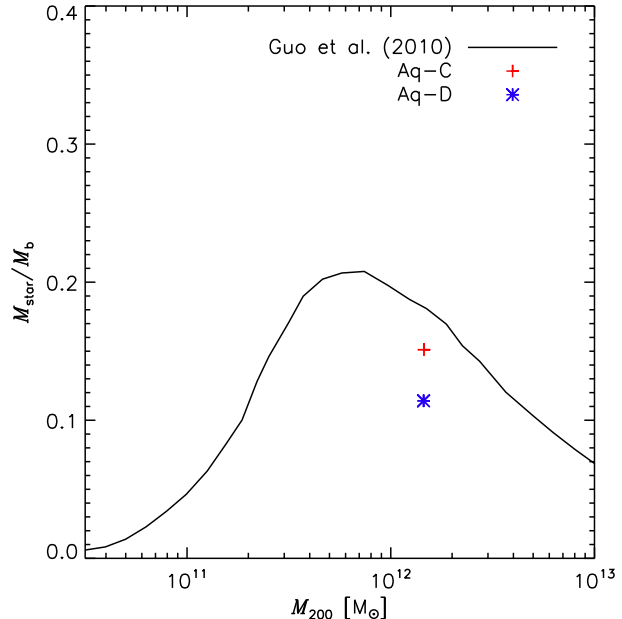


Figure A2. Star formation efficiency as a function of halo mass. The vertical axis shows how many baryons in the halo locked into stars, where $M_b \equiv (\Omega_b/\Omega_0)M_{200}$ and M_{200} is the mass of a sphere whose mean density is 200 times the critical density. The black curve is taken from Guo et al. (2010), which indicates the values required if a Λ CDM universe is to fit the observed SDSS stellar mass function. The red plus sign and blue asterisk indicate the values for Aq-C and Aq-D, respectively.

many baryons into stars (see also Scannapieco et al. 2012). The values for our simulated galaxies are slightly lower than that obtained for the SDSS galaxies by Guo et al. (2010) but they are broadly consistent with their result considering the fact that there must be significant halo-to-halo variation. The galaxy formation efficiency in Aq-D is lower than that in Aq-C since the formation redshift of Aq-D's host halo is more recent and the depth of its potential well is shallower (Springel et al. 2008); therefore the feedback is more efficient for Aq-D.

APPENDIX B: NUMERICAL CONVERGENCE

In order to conduct convergence studies, we also simulated the Aq-C halo at two lower resolutions with particle masses ~ 8 and ~ 64 times larger. Here we employ the same naming convention as Aquarius, labelling the three runs (in order of decreasing resolution) Aq-C-4, Aq-C-5 and Aq-C-6. Aq-C-4 is the one we have called 'Aq-C' in the main text of

Table B1. Numerical parameters employed for the three different resolution simulations: dark matter and SPH particle masses and the gravitational softening length in physical units. The gravitational softening length is kept in constant in comoving units until redshift 3 and then fixed in physical units, i.e. the values shown in the table.

	$M_{\text{DM}} (M_{\odot})$	$M_{\text{SPH}} (M_{\odot})$	$\epsilon_{\text{phys}} (\text{pc})$
Aq-C-4	2.6×10^5	5.8×10^4	257
Aq-C-5	2.1×10^6	4.7×10^5	514
Aq-C-6	1.7×10^7	1.7×10^7	1028

the paper. Table B1 lists the numerical parameters of each simulation.

The only physical parameter that depends on the numerical resolution is the star formation threshold density, n_{th} . The star formation threshold density for Aq-C-4, -5, and -6 are $n_{\text{th}} = 0.1, 0.4,$ and 1.6 cc^{-1} , respectively. A factor of 4 higher density is adopted for a factor of 8 higher mass resolution. This scaling is chosen since, for irradiated nearly isothermal gas with an isothermal density profile, halving the gravitational softening length will increase the maximum density that is resolved by a factor of 4.

Using the same set of the simulations, convergence studies on the satellite population was carried out by Parry et al. (2012) and they found reasonably good convergence of various key properties of the simulated satellite galaxies; such as star formation histories, mass of the satellites and luminosity functions. Comprehensive convergence studies on the central galaxy were presented in Scannapieco et al. (2012) but only Aq-C-5 and Aq-C-6 were used.

In Fig. B1, we show the star formation histories of these galaxies. The results from three different simulations agree quite well, although there are some differences in the differential star formation histories during the starbursts. Such level of difference will occur even if we only change a seed for a random number sequence because of stochasticity of the star formation.

In order to compare the morphologies of the galaxies, we analyse the distribution of the orbital circularity, defined below, of stars in the host haloes. We exclude stars belonging to the satellites. For each star lying within r_{vir} , we compute j_z , the component of specific angular momentum parallel to the z -axis. We then compute the specific angular momentum, $j_c(E)$, of a prograde circular orbit with the same binding energy as the particle in question. The ratio $j_z/j_c(E)$ defines the orbital circularity (Abadi et al. 2003; Okamoto et al. 2005). The way to compute this quantity is described in Okamoto et al. (2010) in detail.

Fig. B2 shows the normalised distributions of the orbital circularity of stars within r_{vir} for three different resolution simulations. We also present that for Aq-D for reference. A cold disc component has $j_z/j_c(E) \simeq 1$ and such a component is evident in all galaxies. There is however no obvious

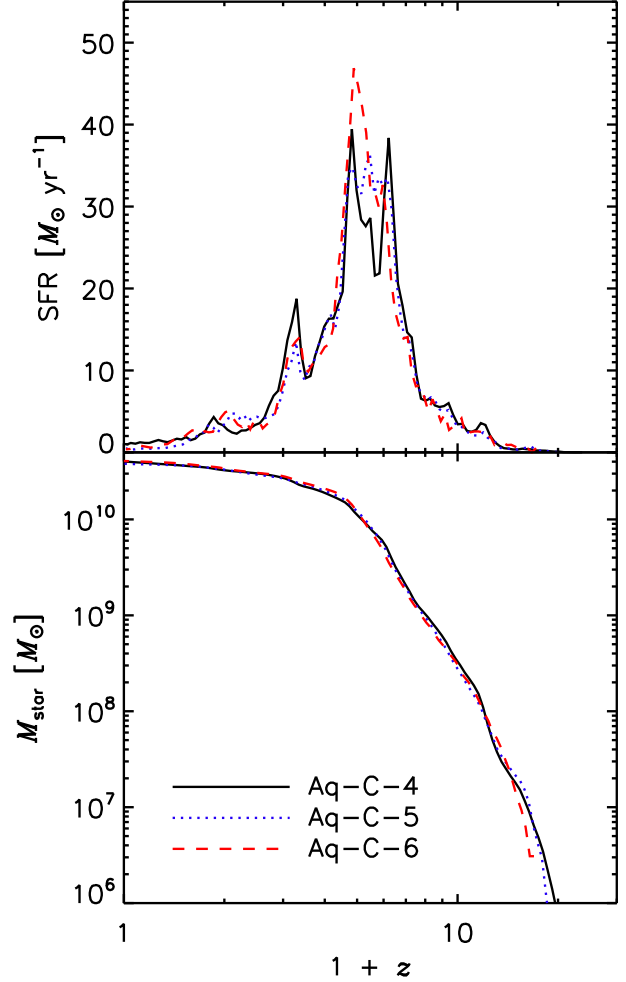


Figure B1. Formation histories of stars within galaxy radius in three different resolution simulations. The upper panel shows the differential star formation histories while the lower panel presents them in cumulative form. The black solid, blue dotted, and red dashed lines corresponds to Aq-C-4, Aq-C-5, and Aq-C-6, respectively.

convergence feature. For example, the fraction of stars with retrograde orbits (i.e. $j_z < 0$) is largest in Aq-C-5; therefore Aq-C-5 is the most spheroid-dominated galaxy of the three⁶. The position of the second highest peak in Aq-C-4 ($j_z/j_c \simeq 0.5$) is different from that in lower resolution counterparts, Aq-C-5 and Aq-C-6 ($j_z/j_c = 0$). Despite the fact that there seems to be no convergence feature, it is encouraging that changing resolution does not totally change the morphology, that is, they all form well-defined discs. By comparing Aq-C-4 with Aq-D, we find Aq-D is more disc dominated than Aq-C-4. This is consistent with the result by the decomposition based on the surface stellar density profiles.

⁶ If we assume the net rotation of a spheroidal component is zero as in Abadi et al. (2003), the mass of a spheroid is given by $2M(j_z < 0)$.

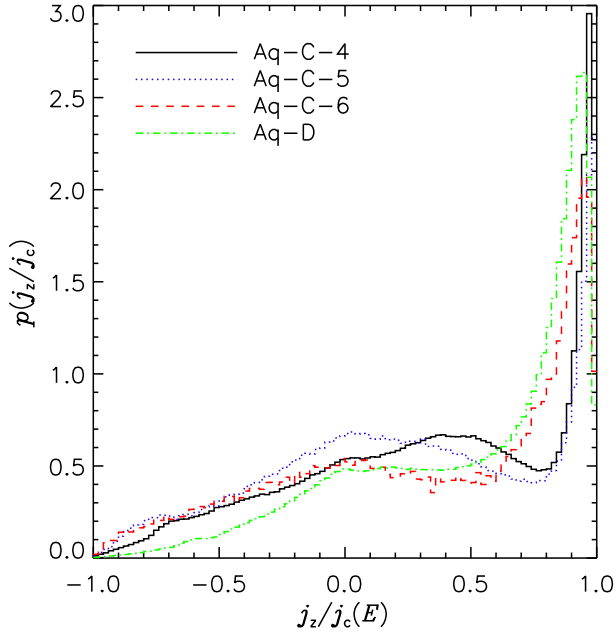


Figure B2. Mass-weighted normalised distribution of orbital circularity, $j_z/j_c(E)$, of all stars lying within r_{vir} of the centre, excluding stars identified as members of satellite galaxies. Aq-C-4, Aq-C-5, and Aq-C-6 are indicated by black solid, blue dotted, and red dashed lines, respectively. For reference, we also show the result for Aq-D (corresponding to the level 4 resolution) by the green dot-dashed line. A peak at $j_z/j_c(E) \simeq 1$ indicates the existence of a disc component.

This paper has been typeset from a \LaTeX file prepared by the author.